Self-assembled nanoflowers from natural building blocks with antioxidant, antibacterial, and antibiofilm properties

SCHOLARONE™
Manuscripts
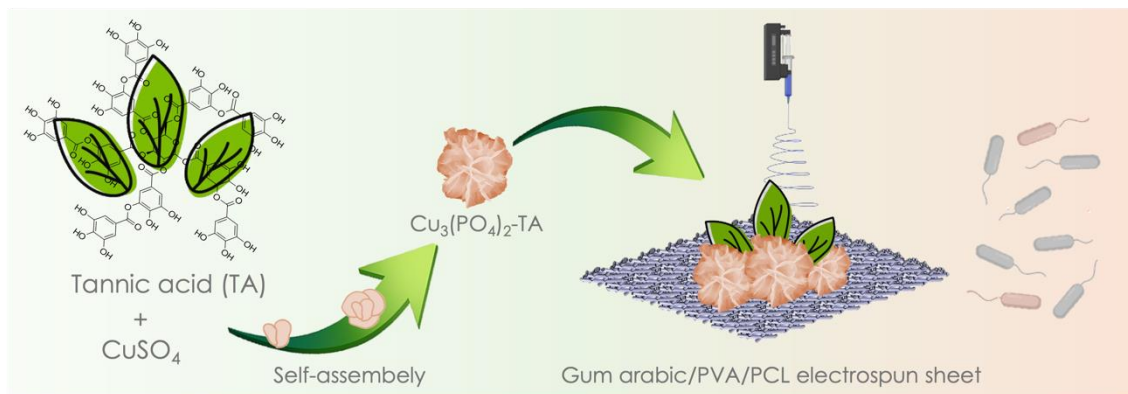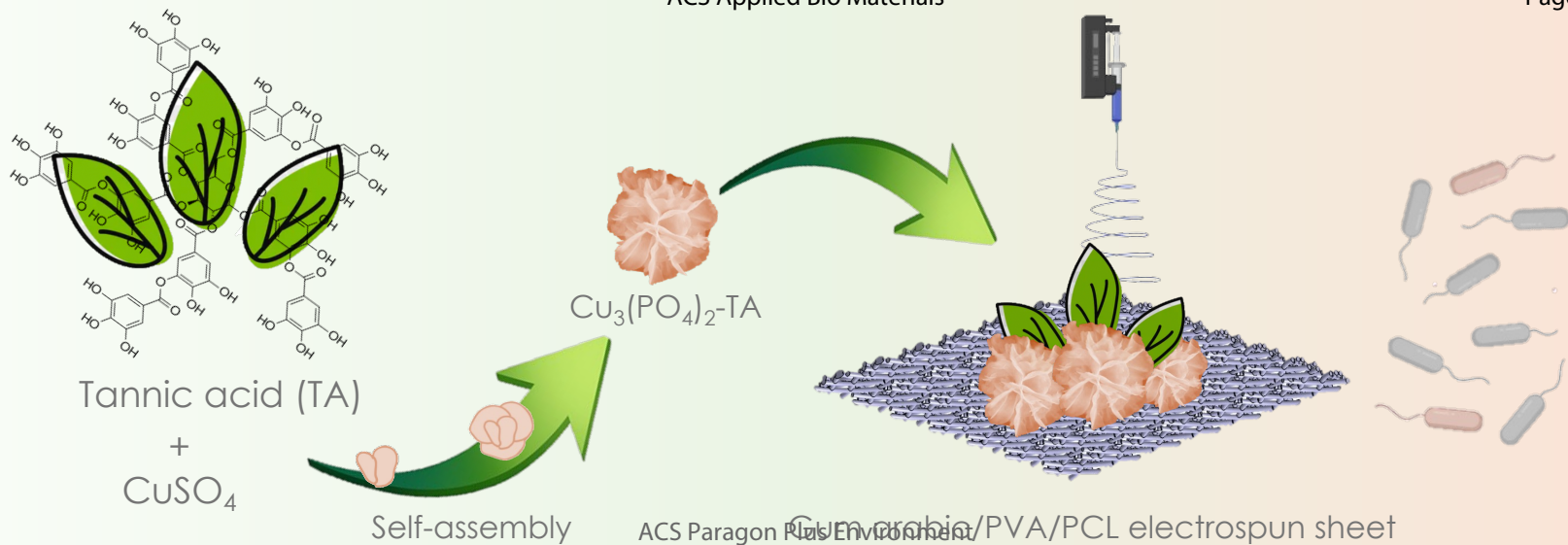
1
2
3
4
5
6
7
8
9
10
11
12
13
14
15
16
17
18
19
20
21
22
23
24
25
26
27
28
29
30
31
32
33
34
35
36
37
38
39
40
41
42
43
44
45
46
47
48
49
50
51
52
53
54
55
56
57
58
59
60

1
2
3
4
5
6
7
8
9
10
11
12
13
14
15
16
17
18

Tannic acid (TA)

+

$CuSO_4$

Self-assembly

$Cu_3(PO_4)_2$-TA

Gum arabic/PVA/PCL electrospun sheet

Self-assembled nanoflowers from natural building blocks with antioxidant, antibacterial, and antibiofilm properties

Fatemeh Ahmadpoor[1], Naeimeh Eghbalifam[2], Paolo Canepa[3], Domenico Palombo[4,5], Patrizia Perego[1,5,6], Pier Francesco Ferrari[*1,5,6]

[1]Department of Civil, Chemical and Environmental Engineering, University of Genoa, via Opera Pia, 15, 16145 Genoa, Italy

[2]Biotechnology Department, Faculty of Chemical Engineering, Tarbiat Modares University, 14115-143 Tehran, Iran

[3]Department of Physics, University of Genoa, via Dodecaneso, 33, 16146 Genoa, Italy

[4]Department of Surgical and Integrated Diagnostic Sciences, University of Genoa, viale Benedetto XV, 6, 16132 Genoa, Italy

[5]Research Center for Biologically Inspired Engineering in Vascular Medicine and Longevity, University of Genoa, via Montallegro, 1, 16145 Genoa, Italy

[6]IRCCS Ospedale Policlinico San Martino, largo Rosanna Benzi, 10, 16132 Genoa, Italy

Abstract

Polyphenols, natural compounds abundant in phenolic structures, have received widespread attention due to their antioxidant, anti-inflammatory, antibacterial, and anticancer properties, making them valuable for biomedical applications. However, the green synthesis of polyphenol-based materials with economical and environmentally friendly strategies is of great significance. In this study, multifunctional wound dressing was achieved by introducing polyphenol-based materials of copper phosphate-tannic acid with flower-like structure (Cu-TA NFs) which shows the reactive oxygen species scavenging performance. This strategy endowed the electrospun wound dressing, composed of poly(caprolactone)-coated gum arabic –poly (vinyl alcohol) nanofibers (GPP), the antibacterial and antibiofilm properties. Our research demonstrates that GPP/Cu-TA NFs are effective against *Staphylococcus aureus*, *Escherichia coli*, and *Pseudomonas aeruginosa*. Furthermore, the developed GPP/Cu-TA NFs showed excellent hemo- and biocompatibility. These results suggest that the synergistic properties of this multifunctional polyphenol platform (GPP/Cu-TA NFs) make it a promising candidate for further development of wound dressing materials.

Keywords: tannic acid; poly(caprolactone); gum arabic, poly(vinyl alcohol); template-free synthesis; nanofiber composite; bioinspired material; wound dressing

1. Introduction

Wound healing and its therapeutic complications have become a crucial healthcare issue, resulting in burdensome economic challenges worldwide. Wounds can be the result of burns, surgeries, abrasions, trauma, and superficial incisions. Chronic wounds can be created by inappropriate treatments or health issues such as diabetes and vascular diseases.[1] In such wounds, the normal regeneration stages of damaged tissue, including hemostasis,

inflammation, proliferation, and remodeling, that re-establish the normal cellular and extracellular composition of the skin, do not occur expectably.[22] In addition, the presence of pathogenic bacteria such as *Staphylococcus aureus*, *Escherichia coli*, and *Pseudomonas aeruginosa*, concurrently with the lack of proper immune function, can inhibit normal wound healing.[3] Bacterial infection is a major concern for wound healing and the treatment with antibiotics has been widely used as the gold-standard protocol in clinical wound care.[4,5] However, the improper and excessive use of antibiotics has been leading to the appearance of a great number of multidrug-resistant (MDR) bacteria.[6] In view of this challenge, it is necessary to develop new antibacterial methods to effectively address the issues of MDR local infections. On the other hand, the difficulty in controlling bacteria is also attributed to biofilm formation, as the relevant studies report that 65% of all bacterial infections present the production of bacterial biofilms.[7] Biofilms consist of bacterial aggregates with extracellular polymeric matrices that attach to the living surface and wound tissue. This matrix acts as a barrier with high resistance against conventional antibiotics.[8] Therefore, infection control has become a research hotspot in the wound healing context. Correspondingly, considerable efforts have been made to develop new antibacterial nanomaterials, including metal and metal oxide nanoparticles[9], carbon-based nanomaterials[10], nanozymes[11], metal-organic frameworks[12], and peptide nanomaterials.[13] However, since the nanomaterials come into direct contact with the wound tissue, the biological safety of those used in wound healing must be considered before any application.[14] Skin irritation and allergy are the most commonly reported transdermal toxicities, attributed to the release of ions and surface coatings which are influenced by factors such as particle size, shape, surface charge, stability, and concentration of nanomaterials.[15] Hence, designing functional materials meeting the biological safety criteria exhibits notable potential for wound healing areas.

Recently, natural molecules have gained great attention in biomaterials due to their potent antioxidative and biocompatibility properties.[16] Among them, polyphenols are a group of heterogeneous chemical compounds found in plant tissues with a wide range of biological functions such as photosynthesis and pigmentation.[17] Tannic acid (TA) is a natural polyphenol compound derived from various plants, composed of a central glucose molecule linked to five digalloyl ester groups. TA contains multiple phenolic groups, which provide interaction binding sites facilitating the organization of constituent particles in the fabrication of functional nanomaterials and bioinspired surface engineering applications.[18] The catechol groups endow TA antioxidant, antibacterial, hemostatic, and anti-inflammatory properties that are beneficial for promoting wound healing.[19]

Carbonyl, phenolic, hydroxyl, and aromatic benzene units of TA have the potential to chemically and physically interact with a variety of organic and inorganic compounds. Notably, the phenolic hydroxyl groups of TA contribute lone pair electrons, facilitating binding with metal ions like Cu^{2+}, Mn^{2+}, Zn^{2+}, Fe^{3+}, Cr^{3+}, and Co^{3+}. These coordination bonds linking the metal ions with the phenolic hydroxyl groups of TA exhibit significant strength and stability. Moreover, TA as an amphiphilic compound can interact with a wide range of materials through hydrophobic interactions, hydrogen bonding, electrostatic interactions, and coordinative bonding.[17] The active chelating sites of TA not only facilitate the localization and conjugation of TA-complex but also protect the antioxidant and reactive oxygen species (ROS) scavenging properties from being inactivated.[20]

Accordingly, in recent years, researchers have focused on applications of TA-based functional materials with synergistic properties for an effective wound dressing capable of accelerating wound healing and possessing antimicrobial properties.[21,22]

Among the materials used for wound dressing, nanofiber-based structures present desired properties such as exudate absorption, high flexibility, oxygen permeability, and large surface area for wound healing.[23] Various methods of nanofiber fabrication, including melt blowing[24],

phase separation[25], self-assembly[26,27], and electrospinning[28], exist, among which, electrospinning is a simple and practical method for producing micro- to nanofibers. The resulting fibers could be utilized in a variety of biomedical applications including tissue engineering scaffolds[29,30], drug delivery[31], and wound dressing.[32] Electrospun nanofiber wound dressings reveal similar structure and biological characteristics to the native extracellular matrix, which provides an ideal environment for cell adhesion, migration, and differentiation. Multiple types of natural, synthetic, and mixed polymers can be utilized for the electrospinning of non-woven nanofibers.[33] Natural polymers such as chitosan, silk, gum arabic (GA), collagen, hyaluronic acid, and dextran are biodegradable and biocompatible; nevertheless, their low cost-effectiveness, weak processability, and poor mechanical properties limit their application as wound dressing materials. Hence, synthetic polymers such as poly (L-lactic acid), poly(lactic-*co*-glycolic acid), poly(vinyl alcohol) (PVA), poly(caprolactone) (PCL), and natural polymers are usually used together to suppress the shortcoming of individual natural polymers and create a suitable wound dressing with enhanced wound healing capabilities.[34,35]

Nanoflowers (NFs), also referred to as three-dimensional hierarchical structures, are organic-inorganic hybrid nanostructures with a flower-like morphology that are synthesized using a bioinspired method. These porous structures have a large surface area and excellent stability that makes NFs useful in different applications, including biosensors, catalysis, and drug delivery.[36] The inorganic component of NFs is mainly composed of metal (Cu, Zn, Ca, Mn, and Co) phosphates, and various organic components like enzymes, proteins, polysaccharides, biosurfactants, DNA, and RNA.[37]

Inspired by the multiple functions of TA in plants, we designed innovative organic-inorganic NFs through the self-assembly of TA and copper phosphate (Cu-TA). In the following sections, we characterized the chemical structure and ROS scavenging of Cu-TA NFs. Besides, Cu-TA NFs were further loaded on the wound dressing that contains both natural and synthetic electrospun nanofibers facilitating the application of such hybrid NF-design systems. Hence, the main objective of this study is to employ the synergistic effect of Cu-TA NFs and electrospun GA/PVA nanofibers coated with PCL for the designation of antibacterial and anti-biofilm wound dressing systems.

2. Materials and Methods

2.1 Materials

Poly(vinyl alcohol) (PVA, M_w = 85,000-124,000 g/mol, 87-89 % hydrolyzed), poly(caprolactone) (PCL, M_w = 80,000 g/mol), 3-(4,5-dimethylthiazol-2-yl)2,5-diphenyltetrazolium bromide (MTT), 2,2-diphenyl-1-picrylhydrazyl (DPPH), 2,2′-azino-bis(3-ethylbenzothiazoline-6-sulfonic acid) (ABTS), and crystal violet were supplied from Sigma-Aldrich (Saint Louis, MO, USA). Gum arabic (GA), chloroform (99.00 - 99.40%), nutrient broth, nutrient agar, dimethyl sulfoxide (DMSO), N–N dimethylformamide (DMF, 99.80%), disodium hydrogen phosphate (Na_2HPO_4), potassium dihydrogen phosphate (KH_2PO_4), sodium chloride (NaCl), potassium chloride (KCl), potassium bromide (KBr), potassium persulfate ($K_2S_2O_8$), were purchased from Merck (Darmstadt, Germany). Tannic acid (TA) was obtained from Alfa Aesar (Haverhill, MA, USA). Isopropanol, Dulbecco's modified Eagle medium (DMEM), and phosphate buffered saline (PBS) were purchased from Carlo Erba (Milan, Italy). Fetal bovine serum (FBS) and penicillin/streptomycin were obtained from Euroclone (Pero, Italy). Formaldehyde was obtained from MML-Medical (Ulf, the Netherlands) as the product BiopSafe®. All the chemicals were utilized as supplied without additional purification and all solutions were prepared using deionized (DI) water.

2.2 Synthesis of Tannic Acid Nanoflowers

To synthesize Cu-TA NFs, 1 mL of a $CuSO_4$ aqueous solution (120 mM) was mixed with 100 mL of PBS (10 mM, pH 7.4) containing 3.0 mg TA and left to incubate for 72 h at ambient temperature ($25 \pm 2°C$) under static conditions. The solution changed from transparent to opaque, indicating the process of nucleation and growth of NFs. Subsequently, the dark green precipitate was collected through centrifugation ($2,856 \times g$, 3 min) (centrifuge from Alliance Bio Expertise MF-20R, Guipry, France), washed with DI water three times, and dried at 70°C.

2.3 Preparation of GA/PVA/PCL Nanofiber Sheet

Nanofiber composite composed of GA, PVA, and PCL was prepared utilizing a combination of electrospinning and coating techniques according to the method by Eghbalifam et al. [38] In brief, 348.0 mg GA (in 3 mL DI water) and 366.0 mg PVA (in 3 mL DMF, at 90°C) were dissolved separately until homogeneous solutions were formed. Then, the produced solutions were mixed and electrospinning was done. The nanofibers were collected on an aluminum foil wrapped around a cylindrical collector. The electrospinning parameters including a feeding rate of 0.5 mL/h, an applied electric voltage of 18.0 kV, a tip-to-collector distance of 150 mm, a rotation speed of the cylindrical collector at 500 rpm, and an electrospinning working time of 12 h were determined through preliminary experiments. Subsequently, the nanocomposite was immersed in the PCL solution (186.0 mg in chloroform) and placed in the oven at 50°C to remove the residual solvent. Upon drying, the coated sheets were peeled off the aluminum foil for further characterization.

2.4 Loading Cu-TA NFs on GA/PVA/PCL Nanofiber Sheet

To deposit Cu-TA NFs onto a GPP nanofiber composite, an adsorption procedure was used. Initially, in order to disperse of Cu-TA NFs in isopropanol, they were sonicated for 30 min. Next, the GPP nanofiber composite was immersed in the solution and shaken for 1 h. Based on the pre-tests, three different amounts of Cu-TA NFs (0, 10, and 20 wt %) were selected.

2.5 Characterization of Nanoflowers and GA/PVA/PCL Nanofiber Sheet

Structural morphology and electron elemental mapping analysis of Cu-TA NFs and GPP-Cu-TA NF composite were conducted by a field emission scanning electron microscopy (FE-SEM MIRA2, TESCAN, Brno, Czech Republic). The X-ray diffraction (XRD) data of Cu-TA NFs were obtained by a PANalytical X'Pert Pro instrument (Eindhoven, The Netherlands) with a copper target (Cu Kα) radiation of 1.5406 Å. Pattern was recorded at diffraction angle from 5 to 80° and a scanning step of 0.02°. Fourier transform infrared (FTIR) spectroscopic analysis was carried out using Spectrum 100 (PerkinElmer, Waltham, MA, USA) in the wavenumber range of 400–4000 cm^{-1} at room temperature with standard KBr pellets. X-ray photoelectron spectroscopy (XPS) measurements were performed using a PHI 5600 Multi-Technique apparatus (Chanhassen, MN, USA). Spectra were acquired with an X-ray Al-monochromatized source (hν 1486.6 eV), a pass energy of 23.50 eV and using a neutralizer to avoid sample charging[39]. Spectra were calibrated by setting the C1s component of adventitious carbon at a binding energy of 284.8 eV. Deconvolution of Cu 2p signal was performed using a 19.9 eV spin-orbit splitting after a Shirley background subtraction.

2.6 Total Antioxidant Activity Measurement (ABTS & DPPH)

The ROS-scavenging activity of Cu-TA NFs and GPP-Cu-TA NFs (10 or 20%) were examined using ABTS and DPPH assays. The ABTS assay was performed following to the protocol of the total antioxidant capacity assay reported by Ferrari et al.[40]. In brief, 7 mM of aqueous solution of ABTS was incubated with 2.45 mM $K_2S_2O_8$ in darkness at room temperature to produce stable ABTS$^{•+}$. Subsequently, the solution was diluted (approximately 1:49, v/v) and

4

adjusted to attain an absorbance of 0.700 ± 0.100 at 734 nm before the test. Following this, 50 µL samples were mixed with 1 mL ABTS solution and allowed to react for 10 minutes at room temperature in the dark. The ABTS radical scavenging activity of GPP, GPP/Cu-TA NFs (10 or 20%) was assessed by adding 1 cm × 1 cm piece of each sample in 1 mL of ABTS solution. The absorbance was recorded at 734 nm after a 10-min incubation at room temperature using a UV–vis spectrophotometer, model Lambda 25 (PerkinElmer, Wellesley, MA, USA).

The capacity of the Cu-TA NFs to scavenge ABTS$^{\bullet+}$ was estimated based on the percentage (%) of inhibition:

$$\text{ABTS}^{\bullet+} \text{ radical scavenging activity (\%)} = \left(1 - \frac{A_s}{A_0}\right) \times 100 \qquad (1)$$

Here, A_s represents the sample absorbance, A_0 refers the absorbance of ABTS solution. The DPPH assay was also performed to evaluate antioxidative ability. Briefly, a freshly prepared DPPH solution at a concentration of 0.058 mM in ethanol and various concentrations of Cu-TA NFs were prepared separately. Next, 3900 µL DPPH solution was mixed with 100 µL of Cu-TA NFs or with a 1 cm × 1 cm piece of GPP, GPP/Cu-TA NFs (10 or 20%) samples and incubated in dark at room temperature for 1 h. Then, corresponding absorbance at 517 nm was measured and the percentage of DPPH scavenging effect was calculated.

2.7 Antibacterial Assay

The antibacterial properties of GPP-Cu-TA NFs against pathogenic microorganisms, *S. aureus* (Gram-positive), *E. coli*, and *P. aeruginosa* (both Gram-negative), were evaluated using the agar diffusion method. Each microorganism was spread on nutrient agar plates with swabs from 0.5 McFarland turbidity standard microbial suspensions which corresponds to an optical density (OD) between 0.08 and 0.1 at 600 nm, approximately equivalent to 1.5×10^8 CFU/mL. The samples were placed in the center of each plate and incubated at 37°C for 24 h. The inhibition zones around the samples were then measured in five directions and the average was calculated.

2.8 Biofilm Inhibition

The antibiofilm activity of GPP/Cu-TA NFs was assessed using crystal violet staining test against *S. aureus*, *E. coli*, and *P. aeruginosa* bacteria. The composite was sterilized with ethanol (99%, *v/v*) and ultraviolet radiation after been placed in 96-well plates. Each well was filled with 180 µL sterile culture medium and 20 µL bacteria solution (10^6 CFU/mL). The plates were incubated at 37°C for 24 h to allow the formation of the biofilm. On the following day, 100 µL of 0.1% (wt) crystal violet was used to stain the wells after the contents were slowly removed and three times rinsed with sterile PBS. After 15-30 min, the wells were washed again with sterile PBS three times and dried. Subsequently, 100 µL of ethanol (99%, *v/v*) was added to each well to dissolve the crystal violet absorbed by the biofilms. The absorbance of the mixed solution was assessed at 595 nm using an microplate reader. The biofilm inhibition was then calculated using the following equation:

$$\text{Biofilm inhibition (\%)} = \left(\frac{\text{OD}_{\text{control}} - \text{OD}_{\text{sample}}}{\text{OD}_{\text{control}}}\right) \times 100 \qquad (2)$$

For the control, wells without GPP/Cu-TA NFs were tested.

2.9 Hemocompatibility Studies

The hemocompatibility of GPP and GPP/Cu-TA NFs was assessed by determining the absorbance of released hemoglobin following the red blood cells (RBCs) lysis. For this assay, whole anti-coagulated fresh blood was obtained from healthy volunteers who have given their consent through an agreement proposed and accepted by a local ethic committee (9 March 2010) whitin the context of "Centro di Risorse Biologiche". Hemolysis experiments were performed in compliance with the Guidelines of the European Community Council in accordance with the Nuremberg Code (Directive 2004/23/EC). Blood samples were collected into ethylenediaminetetraacetic acid test tubes and used within 2 h of collection. To isolate RBCs, 20 mL of PBS buffer was added to 10 mL of whole blood and the mixture was centrifuged at $1,500 \times g$ for 6 min (centrifuge SL 8, Thermo Fisher Scientific, Osterode am Harz, Germany) after gentle mixing. Next, the supernatant was discarded and the same volume of fresh PBS was added to follow the same protocol. The procedure was repeated 5 times with 1:2 ratio of the RBCs to the PBS. Then, RBCs were diluted in fresh PBS to achieve a final concentration of 5% (v/v). Dried GPP and GPP/Cu-TA NFs were mixed with this RBC final suspension and after incubating at room temperature for 15 min, 30 min, 2, 3, 4, 5, and 6 h, the samples were centrifuged at $850 \times g$ for 7 min (centrifuge Z 216 MK, HERMLE Labortechnik GmbH, Wehingen, Germany). Following this, 150 µL of the supernatants were transferred to a 96-well plate and the absorbance of the samples was measured at 540 nm using a plate reader (Labsystems iEMS Reader MF9, Labsystems, Helsinki, Finland). The percentage of non-hemolysis was calculated for each sample using the following equation:

$$\text{Non-hemolyzed RBCs (\%)} = 1 - \frac{(As - An)}{(Ap - An)} \times 100 \qquad (3)$$

Here, A_s represents the sample absorbance, A_n refers the absorbance of negative control, and A_p indicates the absorbance of the positive control. For this assay, PBS and DI water were utilized as the negative and positive control, respectively.

To assess the morphological changes in RBCs following treatment with GPP and GPP/Cu-TA NFs, 0.5 mL of a 5% (v/v) RBC suspension was mixed with the samples and incubated at 37°C for 6 h. The resulting samples were then centrifuged at $850 \times g$ for 7 min with the same centrifuge reported above and fixed in 4% formaldehyde at room temperature for 2 h. Subsequently, the treated RBCs underwent dehydration through sequential immersion in ethanol solutions of increasing concentrations (50, 60, 70, 80, 90, and 99.7%) for 5, 10, 15, 20, 25, and 30 min, respectively. After dehydration, RBC suspensions were dropped onto coverslips, air-dried, sputter-coated with gold, and observed through SEM (model S-2500, Hitachi, Tokyo, Japan). A commercial gauze was used as reference material.

2.10 *In vitro* Cell Viability

To evaluate *in vitro* cytotoxicity effect of the GPP/CuTA NF composite on mouse embryonic fibroblast (MEF) cells and human HaCaT keratinocytes, the 3-(4,5-dimethylthiazol-2-yl)-2,5-diphenyltetrazolium bromide (MTT) assay was performed. For experiments with fibroblasts, 96-well culture plates were seeded with 1×10^4 MEF cells per well for each sample in DMEM containing 15% (v/v) FBS and 1% (v/v) penicillin/streptomycin in 5% CO_2 at 37°C. For tests with keratinocytes, 1.5×10^4 HaCaT cells were seeded per each well in DMEM containing 10% (v/v) FBS in 5% CO_2 at 37°C. The control wells, containing culture medium without nanocomposites, resulting in 100% of cell viability for the two studied cell lines. The MTT assay was conducted with five replicates for each sample, and after 1, 3, 5, and 7 d of incubation, working with MEF cells, and 1, 3, and 4 d of incubation, in the case of HaCaT. In details, 150 µL of fresh medium containing MTT solution was added to each sample after

removal of the exhausted medium and incubated for 3 h at 37ºC to allow the production of formazan dye in the living cells. Then, DMSO was added to each well, and 100 μL of each sample was transferred to another 96-well plate. Finally, the cell viability of the samples was measured at a wavelength of 492 nm using the same microplate reader reported above. Cell viability was determined as the following:

$$Cell\ viability\ (\%) = \frac{Abs_{492}\ (treated\ cells)}{Abs_{492}\ (control\ cells)} \times 100 \qquad (4)$$

2.11 Statistical Analysis

Experiments were performed at least in triplicate and the data are expressed as mean values and standard deviations. The relevant differences among the samples were evaluated using analysis of variance (ANOVA) and Tukey's honestly significant difference (HSD) post-hoc test ($p < 0.05$). The Statistica v. 8.0 software (StatSoft, Tulsa, OK, USA) was used for data processing.

3. Results and Discussion

3.1. Synthesis and Characterization of Cu-TA NFs

The schematic diagram illustrating the preparation of Cu-TA NFs is shown in Figure 1a. Flower-like nanostructures are formed by self-assembly of tannic acid-copper phosphate crystals during incubation. The formation of Cu-TA NFs self-assembly involves nucleation and growth stages. Initially, primary crystals of copper phosphate forming as copper ions interact with phosphate anions in the PBS solution. Then, TA binds to copper phosphate crystals through hydroxyl groups and copper ions interaction leading to the nucleation of nanopetals. Finally, nanopetals grow *via* Cu-TA complex and TA acting as a binding agent, resulting in the formation of porous carnation-like structure.
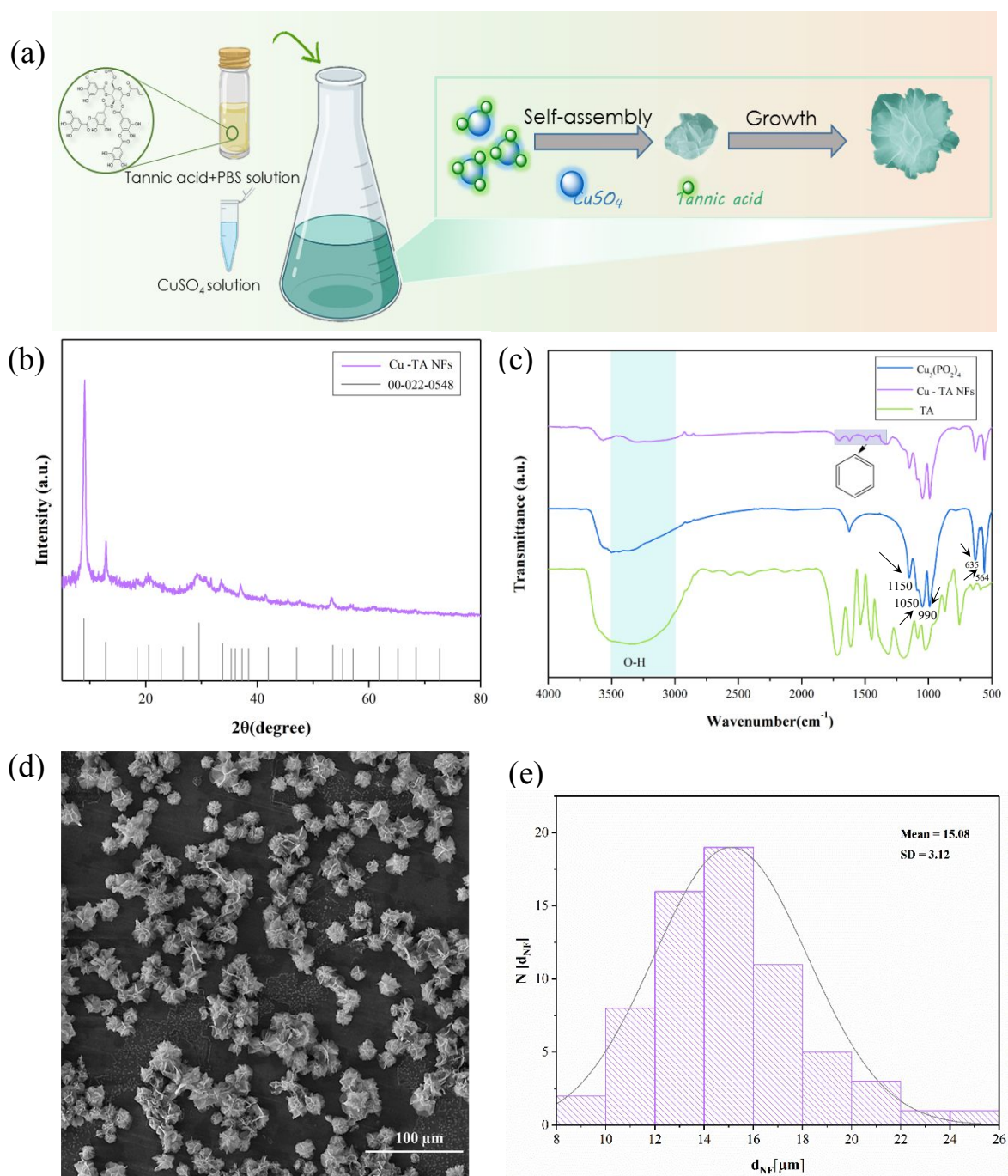
(a)

(b)

(c)

(d)

(e)

Figure 1. Preparation and characterization of the Cu-TA NFs. (a) Schematic illustration for the synthesis of Cu-TA NFs. (b) XRD pattern. (c) FTIR spectra of $Cu_3(PO_4)_2$, Cu-TA NFs, and TA. (d) Representative SEM micrograph of Cu-TA NFs. (e) Size distribution histogram of Cu-TA NFs.

The XRD pattern of the Cu-TA NFs, presented in Figure 1b, was utilized to assess the crystallinity and phase purity of the synthesized products. The results of the XRD analysis indicate that the position and relative intensities of diffraction peaks closely match with those found in the standard $Cu_3(PO_4)_2 \cdot 3H_2O$ (JCPDS 00-022-0548), which confirms that the NFs were highly crystalline and well-formed.

The chemical structures of TA and Cu-TA NFs were assessed by FTIR spectroscopy (Figure 1c). The FTIR spectrum of the Cu-TA NFs displays the characteristic peaks of TA and copper phosphate. The absorption peaks at 1150, 1050, and 990 cm^{-1} are due to the bending vibration of Cu-OH and stretching vibrations of P-O and P=O, respectively. The peaks at 564 and 635 cm^{-1} are assigned to the bending vibration of bridging phosphorous such as O=P-O, confirming the presence of phosphate groups. TA displays a wide band of stretching vibration of OH groups at approximately 3000–3500 cm^{-1}. In addition, an absorption band at about 1200 cm^{-1} is observed, attributed to the bending vibration of OH groups. Furthermore, TA shows two peaks at 1365 and 1616 cm^{-1} which correspond to C-O stretching of the benzene ring and the C=C groups in the aromatic rings, respectively.[41] In the Cu-TA NF spectrum, the shifted peaks and lower intensity of peaks at 648, 1315, and 1189 cm^{-1}, compared to the same region in the TA spectrum, is attributed to combination of factors including the oxidation of polyphenols, as well as cation-π interactions such as coordination bonding between copper ions and phenolic hydroxyl groups, indicating distortion of TA due to the coordination of phenolic groups with copper ions.[42,43]

Figure 1d is related to the SEM micrograph of Cu-TA NFs, which show their flower-like structure. According to this Figure, the Cu-TA NFs exhibited a hierarchical carnation morphology assembled from hundreds of nanopetals with a mean size of 15.08 ± 3.12 μm. The size distribution histogram indicates uniform and a relatively narrow range of NFs (Figure 1e).
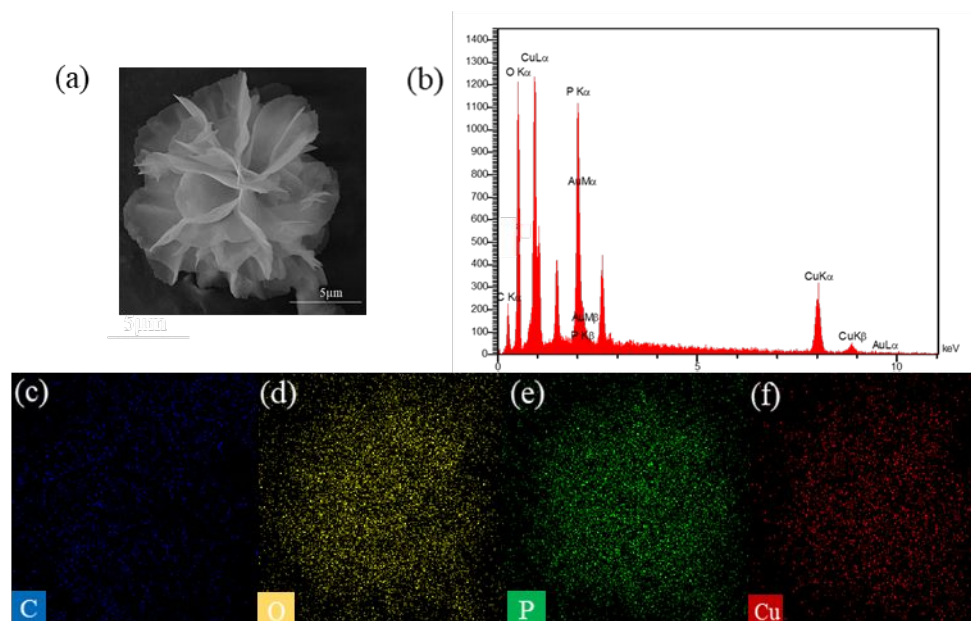

9

Figure 2: Characterization of the synthesized Cu-TA NFs. (a) Representative SEM micrograph of a single Cu-TA NF. (b) EDX spectrum of Cu-TA NF and EDX mappings of the elements (c) C, (d) O, (e) P, and (f) Cu.

The shape, size, and the surface structure of Cu-TA NFs were characterized by SEM (Figure 2). The EDX pattern of the NFs in Figure 2b confirmed the formation of TA-inorganic hybrid structure in the resultant product, as evidenced by the appearance of a C peak. Furthermore, the elemental mapping revealed uniform dispersion of C, O, P, and Cu throughout the Cu-TA NFs (Figure 2c, 2d, 2e, and 2f).

To better study the elemental composition of the Cu-TA NFs and the coordination of the TA with the NFs, we leveraged on the XPS capability to reveal spectral shifts an elemental signal associated to elements in different chemical states of the elements.
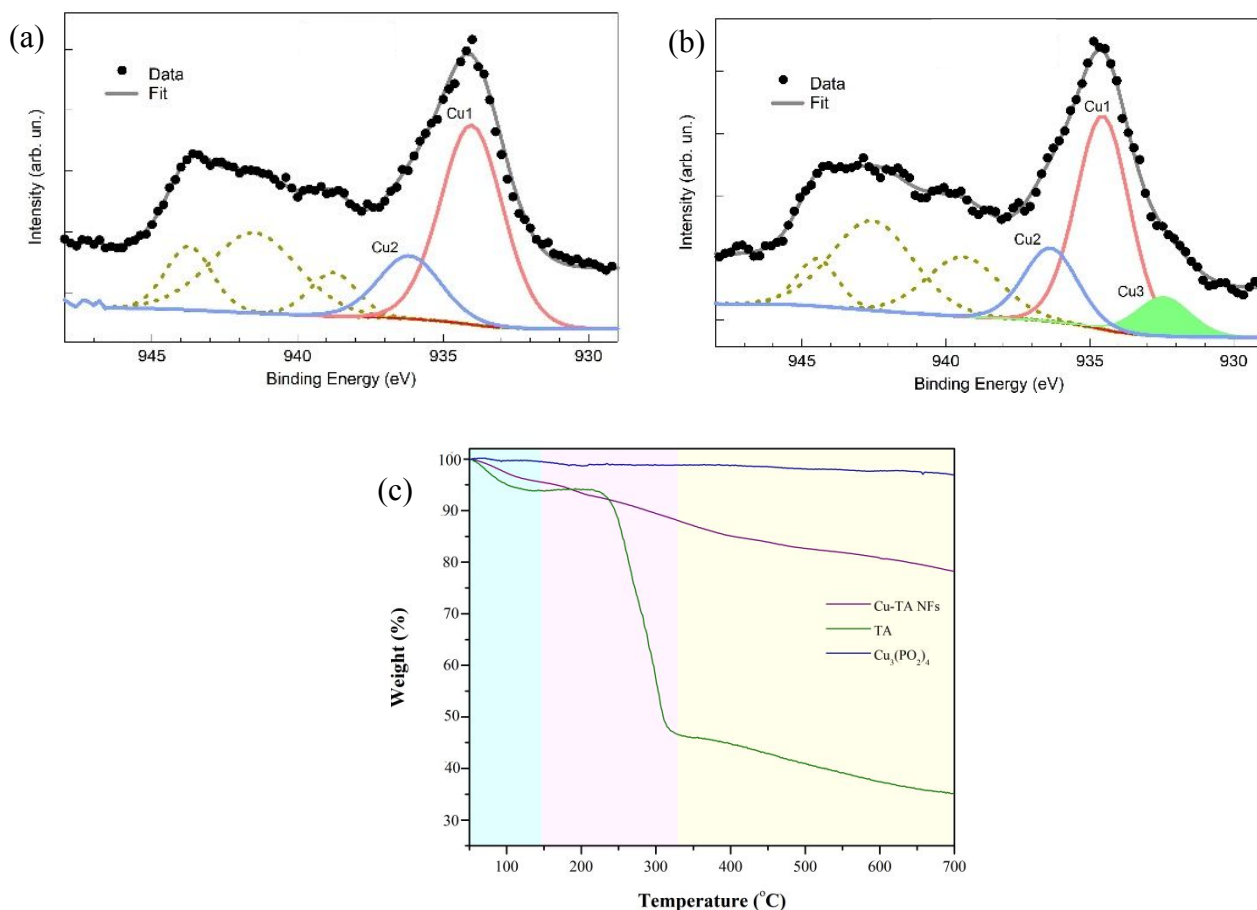
Figure 3. Cu 2p$_{3/2}$ core level XPS spectra of (a) NFs prepared without TA and (b) Cu-TA NFs. (c) TGA analysis of TA, Cu$_3$(PO$_4$)$_2$, and Cu-TA NFs.

The comparison of the Cu 2p$_{3/2}$ spectra of NFs prepared without (Figure 3a) and with TA (Figure 3b) shows the effect of TA on the chemical state of Cu in NFs. A first inspection of the spectra reveals the appearance of two main components (Cu1, red line and Cu2, blue line) in

10

the spectrum of NFs prepared without TA and the appearance of a third component (Cu3, green area) in the signal of Cu-TA NFs.

The deconvolution of the XPS spectrum of the Cu $2p_{3/2}$ core level region of the NFs without TA is reported in Figure 3a (the Cu 2p1/2 components are omitted for an easier figure reading). The main component at a binding energy of (934.1 ± 0.2) eV (Cu1) can be assigned to CuO while the second component at a binding energy of (936.2 ± 0.2) eV (Cu2) derives from the contribution of both $Cu_3(PO_4)_2$ and Cu (OH)$_2$. [44] The other three peaks at binding energies of (939.4 ± 0.2) eV, (942.6 ± 0.2) eV, and (944.5 ± 0.2) eV can be attributed to satellites peaks of Cu^{2+} further confirming the presence of CuO.[45]

Considering the Cu $2p_{3/2}$ core level region of the Cu-TA NFs (reported in Figure 3b), the deconvolution of the main signal needs an additional component Cu3 at a binding energy of (932.4 ± 0.2) eV. This component, not present in NFs prepared without TA, can be attributed to Cu_2O[44].

The TA triggered variation in the chemical state of copper is attributable to the successful coordination of TA with the copper of the NF main structure. The presence of different oxidative states of copper and the changes in the Cu $2p_{3/2}$ signal due to the copper-TA interaction have been already observed by other groups as evidence of the coordination between copper and TA.[42,46]

Spectral changes after coordination with TA were observed also in the C1s and O1s core level regions (data not shown). However, since oxygen and carbon are always present as adventitious contaminants on air exposed surfaces, adventitious C1s and O1s components contribute to the spectra hampering spectra deconvolution.

The thermogravimetric curves of TA, $Cu_3(PO_4)_2$, and Cu-TA NFs were also investigated, shown in Figure 3a. Overall, the mass loss of pure Cu NFs is lower than that of the Cu-TA NFs in the range of 50–700°C. The difference in value of the mass loss is calculated to be 18.67%. The thermal decomposition of Cu-TA NFs can be divided into three main steps. The initial degradation, occurring at temperatures up to 150°C, resulting in a 5% mass loss, attributed to the elimination of water. The major degradation of TA occurred at around 250°C and is attributed to the elimination of decarboxylation products of TA including carbon dioxide, 1,2,3-benzenetriol, and 1,2-benzenediol.[47] In the next step (350–750°C) of thermal degradation, aromatic compounds and carbon dioxide were released due to the degradation of phenolic molecules[48]. Additionally, the coordination of TA to Cu^{2+} enhanced its thermal stability.

3.1.2. ROS Scavenging Activity

Excessive expression and accumulation of ROS can disrupt signaling pathways in cells and induce damage to biomacromolecules, leading to various acute and chronic diseases. Consequently, the removal of free radicals by bioactive substances is crucial for living organisms.[49] Therefore, we assessed the capability of Cu-TA NFs to serve as an effective scavenger of multiple radicals. DPPH and ABTS are commonly used nitrogen-free radicals employed as model molecules to evaluate the ROS scavenging capacity of biomaterials.

The scavenging mechanisms of DPPH˙ rely on capturing one or more hydrogen atoms from antioxidants. As this process occurs, its characteristic color gradually fades, leading to the disappearance of the absorption peak. The results show DPPH radical scavenging activity in the order of TA > Cu-TA NFs > $Cu_3(PO_2)_4$. The superior DPPH radical scavenging activity of TA (Figure S1) can be attributed to the presence of free phenolic -OH groups, which can

11

directly provide hydrogen atoms to reduce DPPH. The presence of Cu-TA NFs leads to an increased scavenging rate at high concentrations. Meanwhile the absorbance of Cu-TA NFs becomes lower than that showed by $Cu_3(PO_2)_4$, demonstrating that they have significantly better scavenging ability and clearance effect (Figure 4b). The original color of DPPH radical was purple which became yellow when it was reduced by an antioxidant. The findings from digital photos further support this conclusion with a noticeable discoloration in their DPPH solutions (Figure S2).

$ABTS^{·+}$ is a widely used and stable nitrogen-free radical with a distinct absorption peak at around 734 nm. The ability of different concentrations of NFs to scavenge $ABTS^{·+}$ was utilized to evaluate the antioxidant capacity of Cu-TA NFs. As depicted in Figure 4c, the absorbance of $ABTS^{·+}$ treated with the Cu-TA NFs decreased significantly, indicating their superior scavenging ability compared to $Cu_3(PO_2)_4$. The Cu-TA NFs demonstrate a concentration-dependent behavior in scavenging $ABTS^{·+}$ (Figure 4d). These results indicate the excellent $ABTS^{·+}$ scavenging activity of Cu-TA NFs.
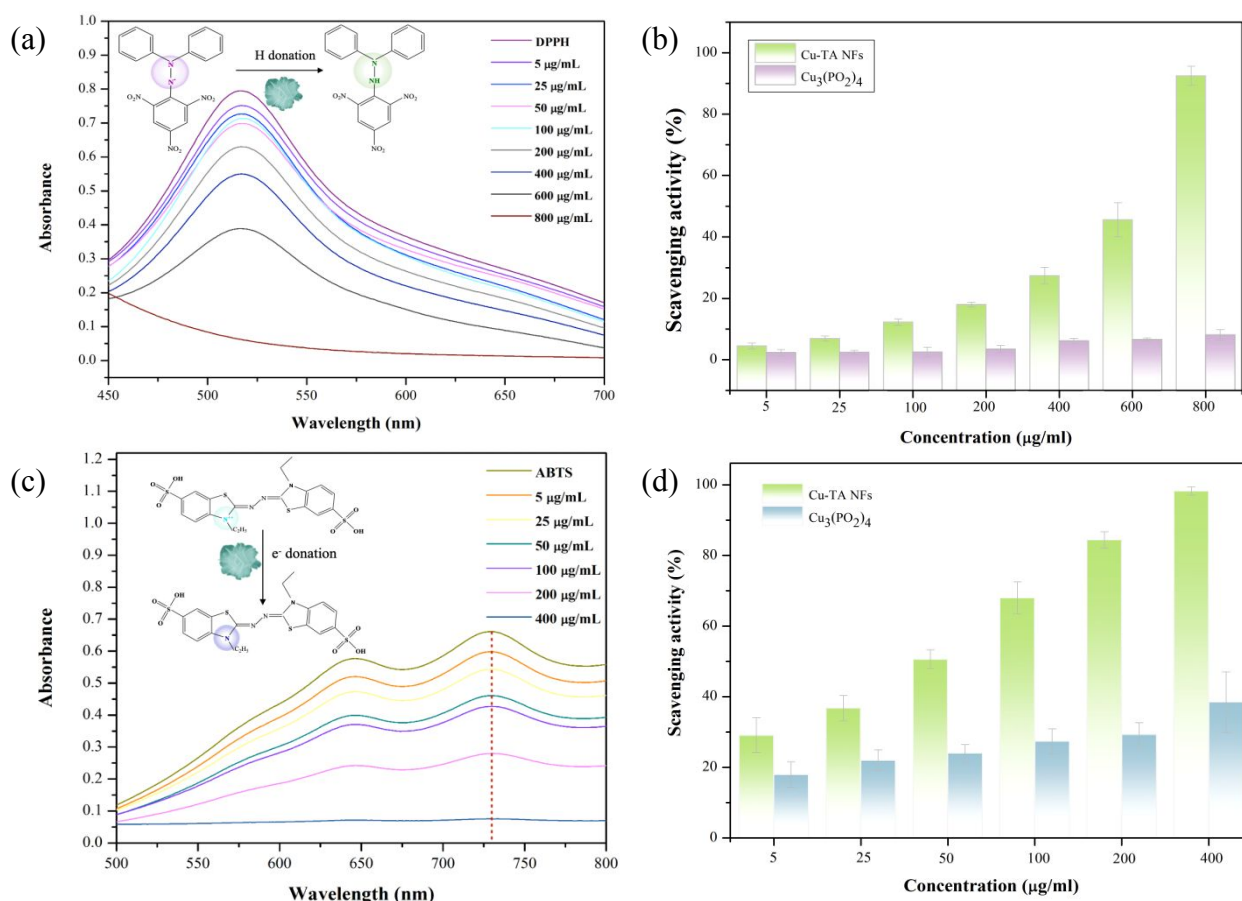
Figure. 4. Assessment of ROS scavenging capacity of Cu-TA NFs. (a) UV−vis spectra of DPPH treated with various concentrations of Cu-TA NFs (5, 25, 100, 200, 400, 600, and 800 µg/mL) for 60 min. (b) DPPH scavenging rate of Cu-TA at the different concentrations. (c) UV−vis spectra of $ABTS^{·+}$ incubated with different concentrations of Cu-TA NFs (5, 25, 50, 100, 200, and 400 µg/mL) for 10 min. (d) $ABTS^{·+}$ scavenging rate of Cu-TA at the different tested concentrations.

3.2 Characterization of GPP/Cu-TA NFs

12

Optimized GA and PVA nanofibers were fabricated by electrospinning method and coated with PCL to improve their hydrophilicity and mechanical properties. The characterization results showed that PCL-coated GA/PVA can be used as wound dressing.[38] Inspired by the high ROS scavenging activity, Cu-TA NFs were loaded on the GPP sheet (Figure 5a). To confirm the critical role of Cu-TA NFs in ROS activity, antibacterial, hemocompatibility, and cell viability properties, we have loaded two concentrations of Cu-TA NFs on GPP sheet. Figure 5b shows the GPP nanofibers with an average of 193 ± 68 nm. SEM micrographs of GPP sheets containing 10 or 20% Cu-TA NFs are displayed in Figure 5c and d. EDX analysis was used to verify the elemental composition of Cu-TA NFs dispersed loaded on GPP nanofibers. Figure 5f shows that the presence of C, O, P, and Cu. Furthermore, the elemental mapping results in Figure 5g indicate elemental C was uniformly distributed throughout the nanofibers. The existence of C, O, P, and Cu can be ascribed to the incorporation of Cu-TA NF on the surface of GPP nanofibers.
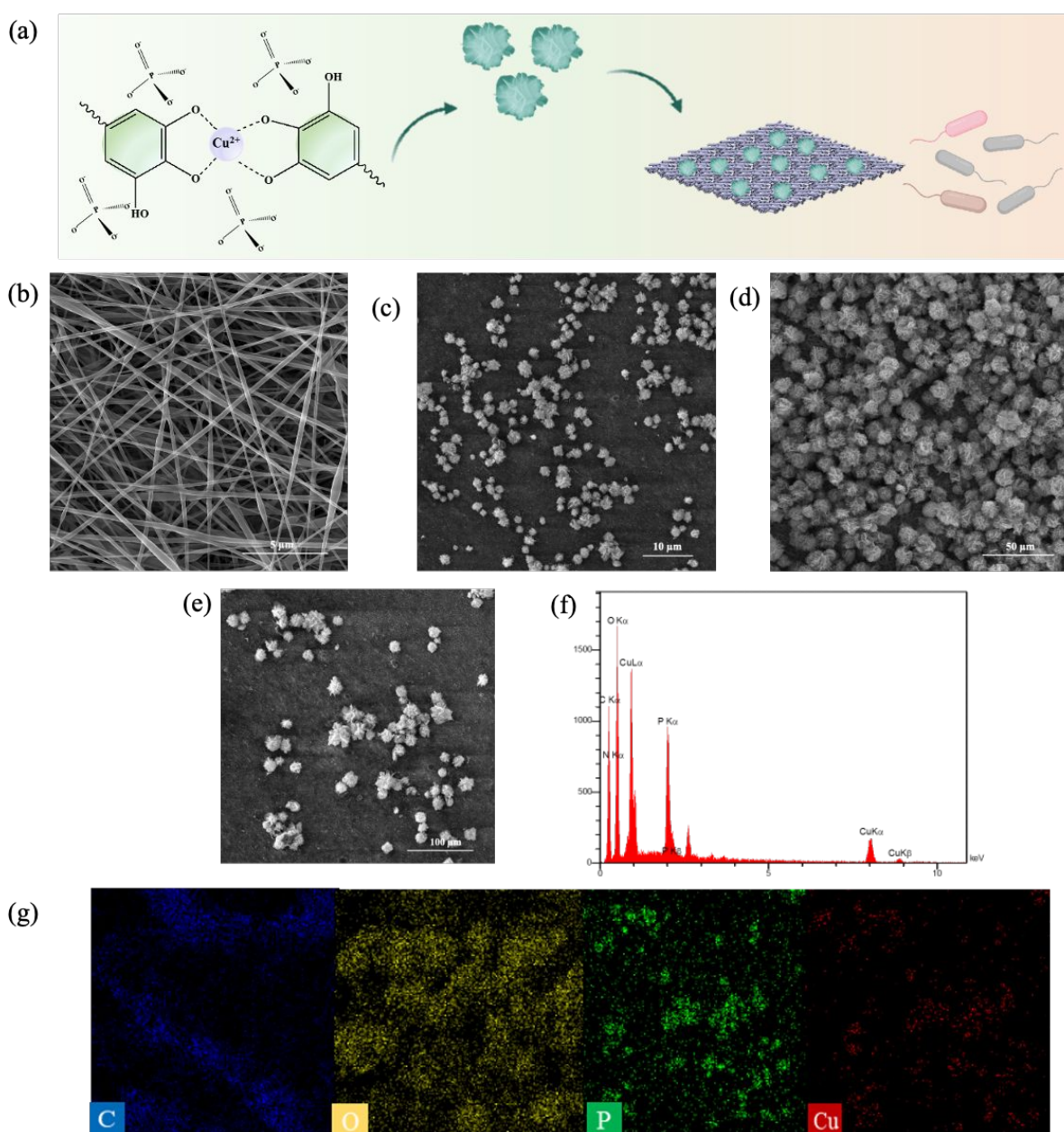
Figure 5: Preparation and characterization of GPP/Cu-TA NFs. (a) Schematic illustration of dispersion Cu-TA NFs on GPP nanofiber sheet. (b) Representative SEM micrograph of GPP nanofiber sheet before and after (c) 10% Cu-TA NFs or (d) 20% Cu-TA NFs. (e) Representative SEM micrograph of GPP/Cu-TA 10%, (f) relative EDX spectrum, and (g) relative EDX mappings of C, O, P, and Cu.

Wound healing is a complex process that encompasses several stages, one of which includes the production of numerous free radicals. Previous studies have indicated that an overproduction of free radicals can disrupt the balance between oxidants and antioxidants, leading to tissue damage, increased infection risk, and delayed healing. Hence, enhancing antioxidant activity is a vital feature of effective wound dressings.[53]

Herein, we tested the ABTS and DPPH scavenging efficiency to evaluate the antioxidant capacity of GPP and GPP/Cu-TA NFs. The free radical scavenging rate increased with the concentration of loaded Cu-TA NFs, with an average of 65.5 and 91.8% of ABTS$^{\cdot+}$ could be scavenged by GPP/Cu-TA NFs at 10 or 20%, respectively (Figure 7a and Figure S3a). The DPPH scavenging efficiency rate of GPP/Cu-TA NFs at 10 or 20% was higher than 48.7 and 65.4%, respectively, significantly higher than that of GPP (5.1%) (Figure 7b and Figure S3b). As in the case of the ABTS assay, a similar trend was observed in this assay also. These data demonstrate that GPP/Cu-TA NFs exhibit strong antioxidant capacity and have great potential for application in wound healing as antioxidant dressings.
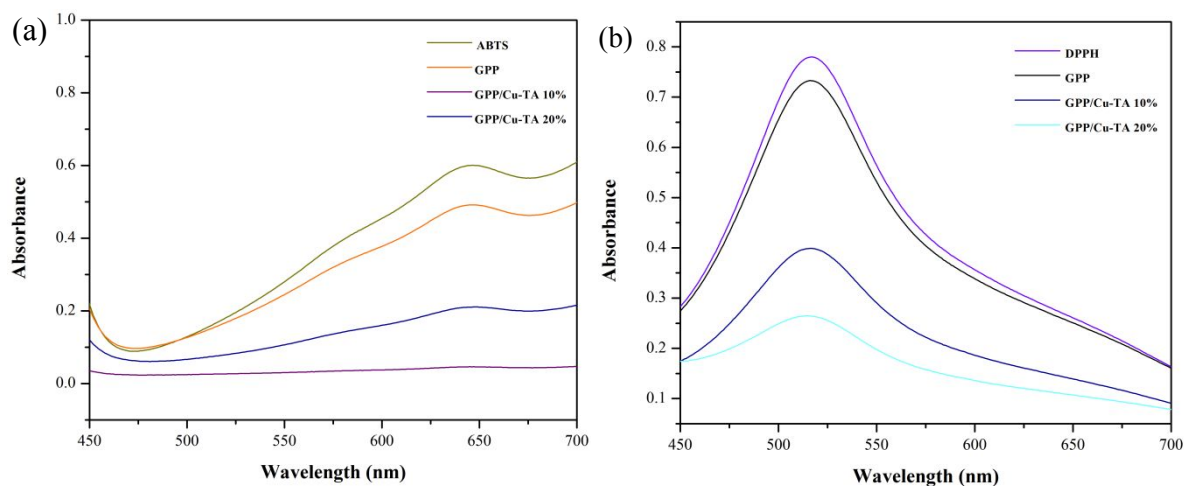

Figure 6: Assessment of ROS scavenging capacity of GPP/Cu-TA. UV−vis spectra of (a) ABTS$^{\cdot+}$ incubated with GPP, GPP/Cu-TA (10%), and GPP/Cu-TA (20%) for 10 min. (b) DPPH treated with GPP, GPP/Cu-TA (10%), GPP/Cu-TA (20%) for 60 min.

3.3. Antibacterial Effect

A suitable wound dressing not only serves as a barrier against external bacterial infections but also possesses inherent antimicrobial abilities, making it significantly more effective in preventing infection.[50] Hence, possessing antibacterial properties is crucial for its clinical application as a wound dressing. The antibacterial activities of GPP loaded with different percentages of Cu-TA NFs were assessed using the inhibition zone method against *S. aureus*, *E. coli*, and *P. aeruginosa*. It was found that the GPP/Cu-TA NFs sheet exhibits a comparable inhibitory effect on both Gram-negative and Gram-positive bacteria. Previous studies have

14

shown the antibacterial properties of TA to be similar against a range of bacteria, including *S. aureus*, *E. coli*, and *P. aeruginosa*, suggesting the potential for its broad-spectrum antibacterial activity. [51]

As illustrated in Figure 7a compared with the control group, the inhibitory effect of the GPP/Cu-TA NFs was positively correlated with the Cu-TA NFs percentage. We could observe dose-dependent manner of NFs because the antibacterial performances of the GPP nanosheet increased when the concentration of Cu-TA NFs was increased from 10 to 20%. The inhibitory zone's average diameter was roughly 18.2 mm for GPP/Cu-TA NFs (20%) sheet in the *S. aureus* cultured agar plate, around 16.4 mm in the *E. coli*, and 14 mm in the *P. aeruginosa*, thereby indicating a higher inhibitory effect on *S. aureus*. The diameters of the bacteriostatic zone were increased from 13.4 to 18.2 mm with increasing the Cu-TA NFs percentage from 10 to 20%. The Gram-positive bacteria (*S. aureus*) are more sensitive to TA than the Gram-negative bacteria (*E. coli* and *P. aeruginosa*) which can may be due to the strong diffusion of TA from Cu-TA NFs. It has been reported that TA effectively eliminates bacteria through multiple mechanisms, including interactions with biomolecules and metal ions within bacterial cells, enhanced permeability of the cell membrane, destabilization of the cytoplasmic membrane, and alteration of the protein-to-lipid ratios within the membrane. It was shown that the hydroxyphenyl group was of great importance against bacterial groups.[52]

Bacterial biofilms are cluster of multiple cells where bacteria are embedded within a matrix of self-produced polymers.[54] The process of biofilm formation includes four stages of adhesion, microcolony formation, biofilm maturation, and detachment or dispersion. This matrix usually shows higher resistance to antimicrobials than cultures grown in suspension (planktonic bacteria). This is due to the low penetration and accumulation of antimicrobials in the biofilm, as well as conditions within the biofilm environment that inactivate antimicrobials.[55] In addition to the protection provided by the matrix, bacteria in biofilms can become hidden from the immune system, causing local tissue damage and eventually leading to acute infections. They can adapt to adverse environmental conditions and nutrient limitations. Moreover, by deactivating antimicrobial agents and reducing cellular function requirements, biofilms increase bacterial resistance to antimicrobial treatment. In biofilm-type infections, the immune system is unable to eliminate the pathogenic biofilm, making these infections persistent and difficult to treat with antimicrobial agents. Consequently, biofilm-related diseases are challenging for the immune system to combat effectively.[56]
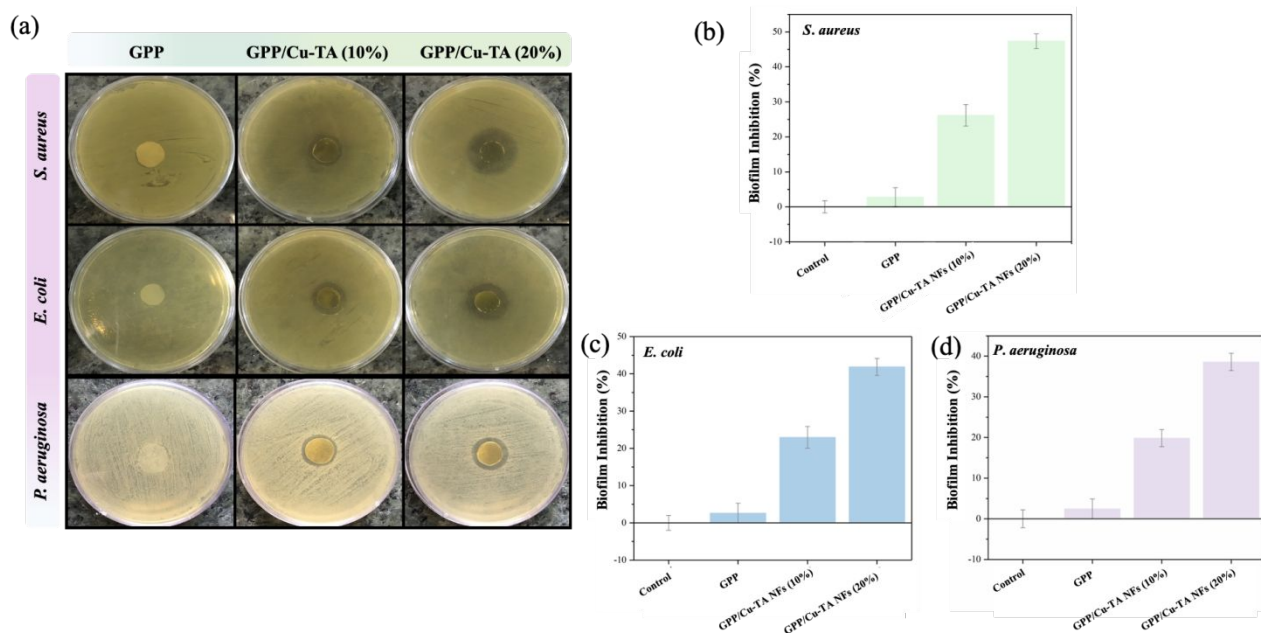
15

Figure 7: Antibacterial activity of GPP/Cu-TA NFs. (a) Antibacterial test of using inhibition zone method against *S. aureus*, *E. coli*, and *P. aeruginosa* after 24 h of incubation. Effect of control, GPP, GPP/Cu-TA (10%), and GPP-Cu-TA (20%) on the biofilm inhibition of (b) *S. aureus*, (c) *E. coli*, and (d) *P. aeruginosa*.

Due to the inherent resilience of biofilm-associated infections, there is a clear need for new antimicrobial agents that specifically target this issue. The ability of GPP/Cu-TA NF sheets to inhibit biofilm formation were assessed using cultures of *S. aureus*, *E. coli*, and *P. aeruginosa* incubated for 24 h. Then, the biofilm was quantified with crystal violet. Cu-TA NFs significantly inhibit the growth of *S. aureus*, *E. coli*, and *P. aeruginosa* in a dose-dependent effect, as shown in Figure 7. As demonstrated, GPP/Cu-TA (20%) NF sheets inhibited biofilm formation by 47, 41, and 38% for *S. aureus*, *E. coli*, and *P. aeruginosa*, respectively (Figure 7b, 7c, and 7d). TA has been recognized for antimicrobial properties and it has been reported to inhibit biofilm formation in highly infection *S. aureus*. [57,58] The findings show that Cu-TA NFs interact with and penetrate to extracellular polymeric substances of the biofilm, eliminating the inner residing bacteria that impede normal bacterial functions and as a result have a breakdown of the biofilm structure.

3.4. Hemocompatibility Studies

Hemocompatibility is a crucial parameter for successful clinical application of materials in direct contact with blood. Hemolysis, the rupture of the RBCs, is a measure to evaluate the hemocompatibility of biomaterials.[59] In accordance with ASTM F756-00 standard, the tested samples can be classified into three groups based on their hemolytic index: (a) materials with hemolysis values higher than 5%, (b) the those exhibiting slight hemolysis with hemolysis values ranging between 2 and 5%, and (c) non-hemolytic materials, demonstrating hemolysis values below 2%.[60] The *in vitro* hemolysis assay was conducted to assess the RBC lysing effect of the GPP, GPP/Cu-TA (10%), and GPP/Cu-TA (20%) at different time intervals (Figure 7a).

In addition, after the centrifugation of the GPP, GPP/Cu-TA (10%), and GPP/Cu-TA (20%) treated RBCs, no samples showed any hemolysis macroscopically (Figure 7b). By contrast, the supernatant was completely transparent red in the positive group (using DI water), revealing complete hemolysis of the RBCs. The results demonstrated that neither GPP nor GPP/Cu-TA (10%), and GPP/Cu-TA (20%) showed obvious hemolysis. Moreover, increasing the Cu-TA concentration from 10 to 20% does not result in a higher hemolysis ratio for GPP/Cu-TA which means this material is suitable for being used as biomedical materials. In addition, to evaluate blood lysis, SEM imaging was employed to assess the possible impact of GPP, GPP/Cu-TA (10%), and GPP/Cu-TA (20%) on the morphological change of the RBCs, as shown in Figure 7c. The RBCs maintained the spherical shape, although, few cells with a star-shaped morphology were observed in SEM images of all samples. The findings indicated that the GPP/Cu-TA did not induce notable changes in the morphology of RBCs after 6 h of treatment.
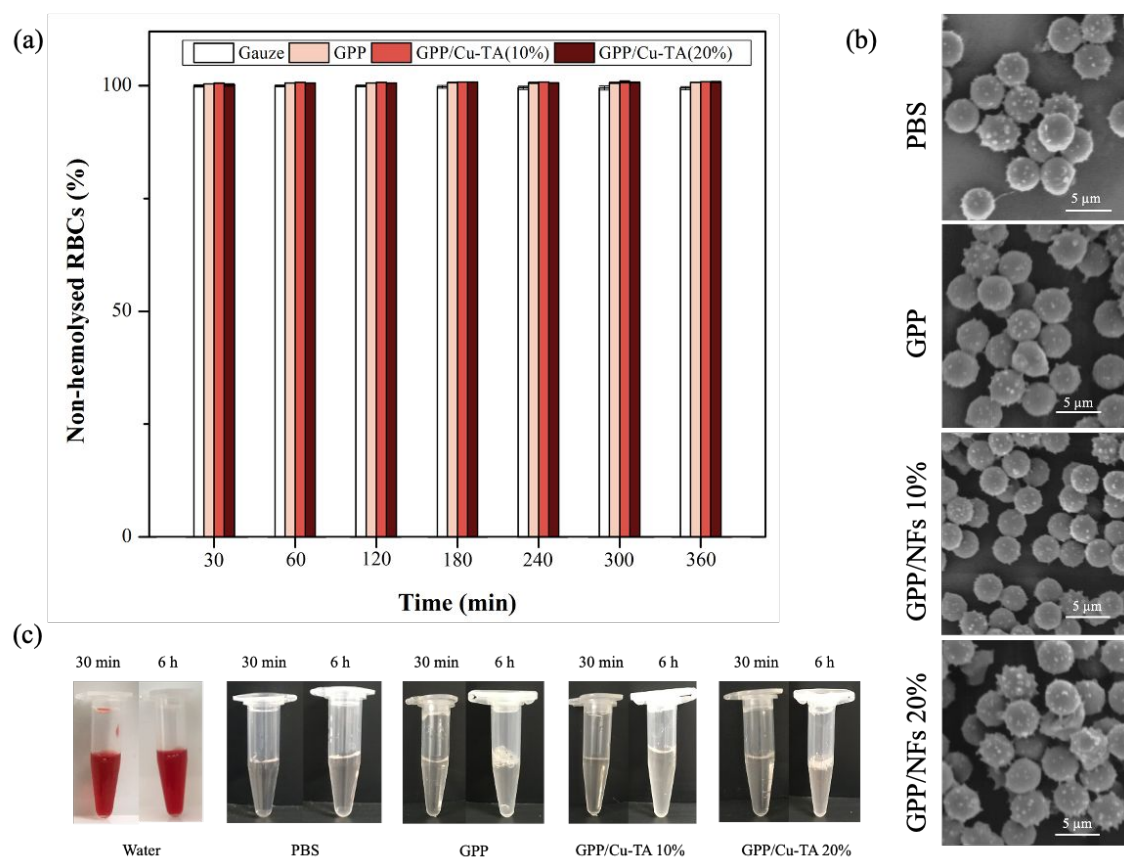
Figure 8: Hemocompatibility of GPP/Cu-TA NFs. (a) Non-hemolyzed ratio of gauze, GPP, GPP/Cu-TA (10%), and GPP/Cu-TA (20%). (b) Assessment of morphological change of the RBCs after 6 h of exposure to GPP, GPP/Cu-TA NFs (10%), and GPP/Cu-TA NFs (20%) by representative SEM micrographs. (c) Representative photographs of RBC supernatants dispersed in water, PBS, GPP, GPP/Cu-TA (10%), and GPP/Cu-TA (20%).

3.5. Cytocompatibility studies

Biocompatibility is an essential factor in the application of electrospun nanofibers in clinical wound dressing. Hence, cell viability was evaluated using MTT assay after a culture of 1, 3, 5,

17

and 7 days for fibroblasts. Generally, the type, shape, size, and surface properties of nanomaterials, as well as the method by which they are incorporated into the sheet, influence their toxicity. Figure 8a summarizes the toxicity profiles of the GPP/Cu-TA NF sheet in fibroblast cells. The results indicated that GPP/Cu-TA NF samples, not only had a biocompatible effect but also enhanced cell proliferation over time. This clearly demonstrates that GPP and Cu-TA NFs promote cell adhesion and growth, as well as showing evidence of Cu-TA NFs are comparable to that of the GPP with cell viabilities exceeding 90%. This shows that the Cu-TA NF concentration used in the composites have no significant difference in cell viability and did not affect the biocompatibility of fibroblasts. Ghuglot et al.[61] investigated cytotoxicity effect of Cu nanoparticles on fibroblast cell viability and the results showed that these nanostructures are not toxic. Du et al.[55] demonstrated that the incorporating of TA into hydrogels, not only enhances cell affinity, but also increases cell adhesion and proliferation and our study aligns with these findings. Considering keratinocytes, cell viability was assessed after 1, 3, and 4 days of incubation. Figure 8b shows all the results obtained, expressed as percentage of cell viability with respect to the control (untreated cells). It was noticed that working with GPP alone and GPP/Cu-TA NFs at the two investigated concentrations, during all the period of treatment resulted in biocompatibility of more than 80%, indicating good biocompatibility of the tested electrospun sheets for these cells. Therefore, it is possible to conclude that GPP/Cu-TA NFs revealed to be cytocompatible at both tested concentration of NFs.
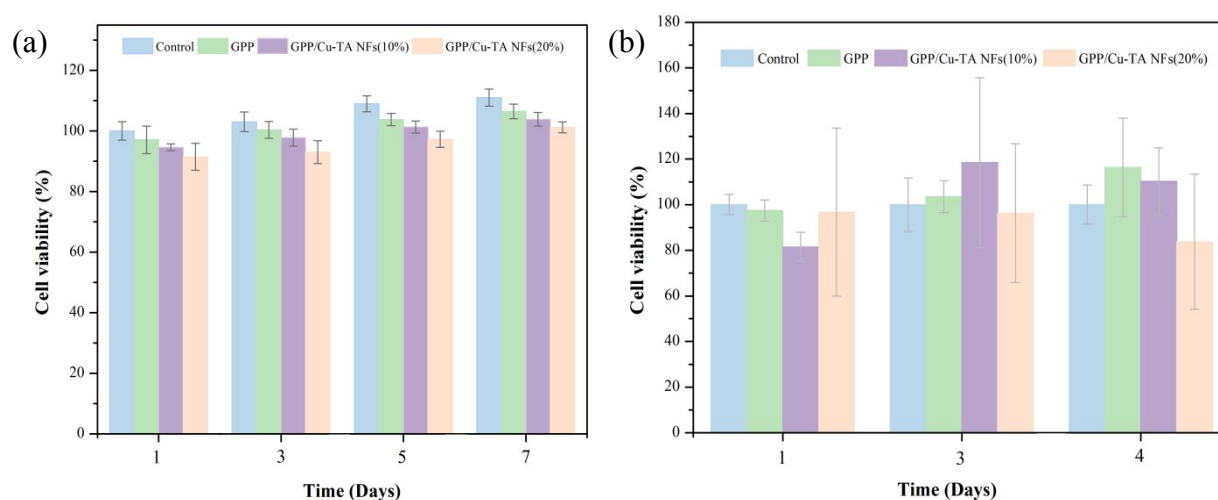

Figure 9: Evaluation of cell viability (a) 1, 3, 5, and 7 days of incubation with fibroblast cells and (b) 1, 3, and 4 days of incubation with keratinocyte cells exposed to control, GPP, GPP-Cu-TA (10%), and GPP-Cu-TA (20%).

4. Conclusion

We used an ecofriendly and simple procedure to create a novel hybrid nanoflower using tannic acid and copper ions as organic and inorganic components, respectively. Facile template-free synthesis endows 3D hierarchical flower-like morphology and porous structure. We loaded these Cu-TA NFs on poly(caprolactone)-coated gum arabic/poly (vinyl alcohol) sheets with different biological properties. Antibacterial experiments confirmed the effect of that GPP/Cu-TA NF sheets on a broad spectrum of bacteria, both Gram positive and negative, and

18

established antibiotic resistant biofilms. Overall, the study presents proof-of-concept evidence for the synthesis and utilization of Cu-TA nanoflowers that open a new avenue as potential material for infection and inflammatory conditions.

Supporting Information

The Supporting Information is available free of charge

at

Figure S1: UV−vis spectra of (a) ABTS$^{.+}$ incubated with different concentrations of TA (5, 25, 50, µg/mL) for 10 min. (b) DPPH treated with various concentrations of TA (3, 5, 50, 75, and 100 µg/mL) for 60 min; Figure S2: Digital photo of changing the color of DPPH solutions with increasing the concentration of Cu-TA NFs from 0 to 800 µg/mL; Figure S3: Assessment of ROS scavenging capacity of Cu-TA NFs. (a) DPPH scavenging rate of GPP sheet. (b) ABTS$^{.+}$ scavenging rate of GPP sheet.

Acknowledgments

References

(1)   Wang, C.; Jiang, X.; Kim, H. J.; Zhang, S.; Zhou, X.; Chen, Y.; Ling, H.; Xue, Y.; Chen, Z.; Qu, M.; Ren, L.; Zhu, J.; Libanori, A.; Zhu, Y.; Kang, H.; Ahadian, S.; Dokmeci, M. R.; Servati, P.; He, X.; Gu, Z.; Sun, W.; Khademhosseini, A. Flexible Patch with Printable and Antibacterial Conductive Hydrogel Electrodes for Accelerated Wound Healing. *Biomaterials* **2022**, *285*, 121479. https://doi.org/10.1016/J.BIOMATERIALS.2022.121479.

(2)   Lisovsky, A.; Chamberlain, M. D.; Wells, L. A.; Sefton, M. V. Cell Interactions with Vascular Regenerative MAA-Based Materials in the Context of Wound Healing. *Adv Healthc Mater* **2015**, *4* (16), 2375–2387. https://doi.org/10.1002/ADHM.201500192.

(3)   Boateng, J. S.; Matthews, K. H.; Stevens, H. N. E.; Eccleston, G. M. Wound Healing Dressings and Drug Delivery Systems: A Review. *J Pharm Sci* **2008**, *97* (8), 2892–2923. https://doi.org/10.1002/JPS.21210.

(4)   Qi, X.; Huang, Y.; You, S.; Xiang, Y.; Cai, E.; Mao, R.; Pan, W.; Tong, X.; Dong, W.; Ye, F.; Shen, J. Engineering Robust Ag-Decorated Polydopamine Nano-Photothermal Platforms to Combat Bacterial Infection and Prompt Wound Healing. *Advanced Science* **2022**, *9* (11), 2106015. https://doi.org/10.1002/ADVS.202106015.

(5)   Tiwari, P.; Gupta, A.; Shukla, D. N.; Mishra, A. K.; Basu, A.; Dutt Konar, A. Chiral Orchestration: A Tool for Fishing out Tripeptide-Based Mechanoresponsive Supergelators Possessing Anti-Inflammatory and Antimicrobial Properties. *ACS Appl Bio Mater* **2021**, *4* (5), 4119–4130. https://doi.org/10.1021/ACSABM.0C01513/ASSET/IMAGES/LARGE/MT0C01513_0009.JPEG.

(6)   Tian, J.; Dong, X.; Eluby, #; Sabola, E.; Wang, Y.; Chen, K.; Zhu, M.; Dai, B.; Zhang, S.; Guo, F.; Shi, K.; Chi, J.; Xu, P. Sequential Regulation of Local Reactive Oxygen Species by Ir@Cu/Zn-MOF Nanoparticles for Promoting Infected Wound Healing. *ACS Biomater Sci Eng* **2024**. https://doi.org/10.1021/ACSBIOMATERIALS.4C00261.

(7)   Jamal, M.; Ahmad, W.; Andleeb, S.; Jalil, F.; Imran, M.; Nawaz, M. A.; Hussain, T.; Ali, M.; Rafiq, M.; Kamil, M. A. Bacterial Biofilm and Associated Infections. *Journal of the Chinese Medical Association* **2018**, *81* (1), 7–11. https://doi.org/10.1016/J.JCMA.2017.07.012.

(8)   Deepika, M. S.; Thangam, R.; Sundarraj, S.; Sheena, T. S.; Sivasubramanian, S.; Kulandaivel, J.; Thirumurugan, R. Co-Delivery of Diverse Therapeutic Compounds Using PEG-PLGA Nanoparticle Cargo against Drug-Resistant Bacteria: An Improved Anti-Biofilm Strategy. *ACS Appl Bio Mater* **2020**, *3* (1), 385–399. https://doi.org/10.1021/ACSABM.9B00850/SUPPL_FILE/MT9B00850_SI_001.PDF.

(9)   Xu, C.; Akakuru, O. U.; Ma, X.; Zheng, J.; Zheng, J.; Wu, A. Nanoparticle-Based Wound Dressing: Recent Progress in the Detection and Therapy of Bacterial Infections. *Bioconjug Chem* **2020**, *31* (7), 1708–1723. https://doi.org/10.1021/ACS.BIOCONJCHEM.0C00297/ASSET/IMAGES/MEDIUM/BC0C00297_0005.GIF.

(10)   Sadat, Z.; Farrokhi-Hajiabad, F.; Lalebeigi, F.; Naderi, N.; Ghafori Gorab, M.; Ahangari Cohan, R.; Eivazzadeh-Keihan, R.; Maleki, A. A Comprehensive Review on the Applications of Carbon-Based Nanostructures in Wound Healing: From Antibacterial Aspects to Cell Growth Stimulation. *Biomater Sci* **2022**, *10* (24), 6911–6938. https://doi.org/10.1039/D2BM01308H.

(11)   Mohammad, M.; Ahmadpoor, F.; Shojaosadati, S. A. Mussel-Inspired Magnetic Nanoflowers as an Effective Nanozyme and Antimicrobial Agent for Biosensing and Catalytic Reduction of Organic Dyes. *ACS Omega* **2020**, *5* (30), 18766–18777. https://doi.org/10.1021/ACSOMEGA.0C01864/ASSET/IMAGES/LARGE/AO0C01864_0008.JPEG.

(12)   Han, D.; Liu, X.; Wu, S. Metal Organic Framework-Based Antibacterial Agents and Their Underlying Mechanisms. *Chem Soc Rev* **2022**, *51* (16), 7138–7169. https://doi.org/10.1039/D2CS00460G.

(13)   Abbas, M.; Ovais, M.; Atiq, A.; Ansari, T. M.; Xing, R.; Spruijt, E.; Yan, X. Tailoring Supramolecular Short Peptide Nanomaterials for Antibacterial Applications. *Coord Chem Rev* **2022**, *460*, 214481. https://doi.org/10.1016/J.CCR.2022.214481.

(14)   Wang, M.; Huang, X.; Zheng, H.; Tang, Y.; Zeng, K.; Shao, L.; Li, L. Nanomaterials Applied in Wound Healing: Mechanisms, Limitations and Perspectives. *Journal of*

20

Controlled Release **2021**, *337*, 236–247.
https://doi.org/10.1016/J.JCONREL.2021.07.017.

(15) Mohanta, D.; Patnaik, S.; Sood, S.; Das, N. Carbon Nanotubes: Evaluation of Toxicity at Biointerfaces. **2019**. https://doi.org/10.1016/j.jpha.2019.04.003.

(16) Vaou, N.; Stavropoulou, E.; Voidarou, C.; Tsigalou, C.; Bezirtzoglou, E. Towards Advances in Medicinal Plant Antimicrobial Activity: A Review Study on Challenges and Future Perspectives. *Microorganisms 2021, Vol. 9, Page 2041* **2021**, *9* (10), 2041. https://doi.org/10.3390/MICROORGANISMS9102041.

(17) Jafari, H.; Ghaffari-Bohlouli, P.; Niknezhad, S. V.; Abedi, A.; Izadifar, Z.; Mohammadinejad, R.; Varma, R. S.; Shavandi, A. Tannic Acid: A Versatile Polyphenol for Design of Biomedical Hydrogels. *J Mater Chem B* **2022**, *10* (31), 5873–5912. https://doi.org/10.1039/D2TB01056A.

(18) Ejima, H.; Richardson, J. J.; Liang, K.; Best, J. P.; Van Koeverden, M. P.; Such, G. K.; Cui, J.; Caruso, F. One-Step Assembly of Coordination Complexes for Versatile Film and Particle Engineering. *Science (1979)* **2013**, *341* (6142), 154–157. https://doi.org/10.1126/SCIENCE.1237265/SUPPL_FILE/EJIMA.SM-CORRECTED.PDF.

(19) Sathishkumar, G.; Gopinath, K.; Zhang, K.; Kang, E. T.; Xu, L.; Yu, Y. Recent Progress in Tannic Acid-Driven Antibacterial/Antifouling Surface Coating Strategies. *J Mater Chem B* **2022**, *10* (14), 2296–2315. https://doi.org/10.1039/D1TB02073K.

(20) Mucha, P.; Skoczyńska, A.; Małecka, M.; Hikisz, P.; Budzisz, E. Overview of the Antioxidant and Anti-Inflammatory Activities of Selected Plant Compounds and Their Metal Ions Complexes. *Molecules* **2021**, *26* (16). https://doi.org/10.3390/MOLECULES26164886.

(21) Bigham, A.; Rahimkhoei, V.; Abasian, P.; Delfi, M.; Naderi, J.; Ghomi, M.; Dabbagh Moghaddam, F.; Waqar, T.; Nuri Ertas, Y.; Sharifi, S.; Rabiee, N.; Ersoy, S.; Maleki, A.; Nazarzadeh Zare, E.; Sharifi, E.; Jabbari, E.; Makvandi, P.; Akbari, A. Advances in Tannic Acid-Incorporated Biomaterials: Infection Treatment, Regenerative Medicine, Cancer Therapy, and Biosensing. *Chemical Engineering Journal* **2022**, *432*, 134146. https://doi.org/10.1016/J.CEJ.2021.134146.

(22) Guo, S.; Ren, Y.; Chang, R.; He, Y.; Zhang, D.; Guan, F.; Yao, M. Injectable Self-Healing Adhesive Chitosan Hydrogel with Antioxidative, Antibacterial, and Hemostatic Activities for Rapid Hemostasis and Skin Wound Healing. *ACS Appl Mater Interfaces* **2022**, *14* (30), 34455–34469. https://doi.org/10.1021/ACSAMI.2C08870/SUPPL_FILE/AM2C08870_SI_001.PDF.

(23) Sylvester, M. A.; Amini, F.; Keat, T. C. Electrospun Nanofibers in Wound Healing. *Mater Today Proc* **2020**, *29*, 1–6. https://doi.org/10.1016/J.MATPR.2020.05.686.

(24) Kamin, Z.; Abdulrahim, N.; Misson, M.; Chiam, C. K.; Sarbatly, R.; Krishnaiah, D.; Bono, A. Use of Melt Blown Polypropylene Nanofiber Templates to Obtain Homogenous Pore Channels in Glycidyl Methacrylate/Ethyl Dimethacrylate-Based Monoliths. *Chem Eng Commun* **2021**, *208* (5), 661–672. https://doi.org/10.1080/00986445.2020.1715958.

(25) Qin, W.; Li, J.; Tu, J.; Yang, H.; Chen, Q.; Liu, H. Fabrication of Porous Chitosan Membranes Composed of Nanofibers by Low Temperature Thermally Induced Phase Separation, and Their Adsorption Behavior for Cu2+. *Carbohydr Polym* **2017**, *178*, 338–346. https://doi.org/10.1016/J.CARBPOL.2017.09.051.

(26) Shin, S.; Menk, F.; Kim, Y.; Lim, J.; Char, K.; Zentel, R.; Choi, T. L. Living Light-Induced Crystallization-Driven Self-Assembly for Rapid Preparation of Semiconducting Nanofibers. *J Am Chem Soc* **2018**, *140* (19), 6088–6094. https://doi.org/10.1021/JACS.8B01954/SUPPL_FILE/JA8B01954_SI_001.PDF.

21

(27) Gavel, P. K.; Kumar, N.; Parmar, H. S.; Das, A. K. Evaluation of a Peptide-Based Coassembled Nanofibrous and Thixotropic Hydrogel for Dermal Wound Healing. *ACS Appl Bio Mater* **2020**, *3* (5), 3326–3336. https://doi.org/10.1021/ACSABM.0C00252/ASSET/IMAGES/LARGE/MT0C00252_0007.JPEG.

(28) Bozkaya, O.; Arat, E.; Gün Gök, Z.; Yiğitoğlu, M.; Vargel, İ. Production and Characterization of Hybrid Nanofiber Wound Dressing Containing Centella Asiatica Coated Silver Nanoparticles by Mutual Electrospinning Method. *Eur Polym J* **2022**, *166*, 111023. https://doi.org/10.1016/J.EURPOLYMJ.2022.111023.

(29) Rahmati, M.; Mills, D. K.; Urbanska, A. M.; Saeb, M. R.; Venugopal, J. R.; Ramakrishna, S.; Mozafari, M. Electrospinning for Tissue Engineering Applications. *Prog Mater Sci* **2021**, *117*, 100721. https://doi.org/10.1016/J.PMATSCI.2020.100721.

(30) Ferrari, P. F.; Aliakbarian, B.; Lagazzo, A.; Tamayol, A.; Palombo, D.; Perego, P. Tailored Electrospun Small-Diameter Graft for Vascular Prosthesis. *International Journal of Polymeric Materials and Polymeric Biomaterials* **2017**, *66* (12), 635–643. https://doi.org/10.1080/00914037.2016.1252361.

(31) Luraghi, A.; Peri, F.; Moroni, L. Electrospinning for Drug Delivery Applications: A Review. *Journal of Controlled Release* **2021**, *334*, 463–484. https://doi.org/10.1016/J.JCONREL.2021.03.033.

(32) Liu, Y.; Li, T.; Han, Y.; Li, F.; Liu, Y. Recent Development of Electrospun Wound Dressing. *Curr Opin Biomed Eng* **2021**, *17*, 100247. https://doi.org/10.1016/J.COBME.2020.100247.

(33) Memic, A.; Abudula, T.; Mohammed, H. S.; Joshi Navare, K.; Colombani, T.; Bencherif, S. A. Latest Progress in Electrospun Nanofibers for Wound Healing Applications. *ACS Appl Bio Mater* **2019**, *2* (3), 952–969. https://doi.org/10.1021/ACSABM.8B00637/ASSET/IMAGES/MEDIUM/MT-2018-006373_0011.GIF.

(34) Juncos Bombin, A. D.; Dunne, N. J.; McCarthy, H. O. Electrospinning of Natural Polymers for the Production of Nanofibres for Wound Healing Applications. *Materials Science and Engineering: C* **2020**, *114*, 110994. https://doi.org/10.1016/J.MSEC.2020.110994.

(35) Yang, S.; Li, X.; Liu, P.; Zhang, M.; Wang, C.; Zhang, B. Multifunctional Chitosan/Polycaprolactone Nanofiber Scaffolds with Varied Dual-Drug Release for Wound-Healing Applications. *ACS Biomater Sci Eng* **2020**, *6* (8), 4666–4676. https://doi.org/10.1021/ACSBIOMATERIALS.0C00674/ASSET/IMAGES/LARGE/AB0C00674_0008.JPEG.

(36) Shcharbin, D.; Halets-Bui, I.; Abashkin, V.; Dzmitruk, V.; Loznikova, S.; Odabaşı, M.; Acet, Ö.; Önal, B.; Özdemir, N.; Shcharbina, N.; Bryszewska, M. Hybrid Metal-Organic Nanoflowers and Their Application in Biotechnology and Medicine. *Colloids Surf B Biointerfaces* **2019**, *182*, 110354. https://doi.org/10.1016/J.COLSURFB.2019.110354.

(37) Perwez, M.; Lau, S. Y.; Hussain, D.; Anboo, S.; Arshad, M.; Thakur, P. Nanozymes and Nanoflower: Physiochemical Properties, Mechanism and Biomedical Applications. *Colloids Surf B Biointerfaces* **2023**, *225*, 113241. https://doi.org/10.1016/J.COLSURFB.2023.113241.

(38) Eghbalifam, N.; Shojaosadati, S. A.; Hashemi-Najafabadi, S.; Khorasani, A. C. Synthesis and Characterization of Antimicrobial Wound Dressing Material Based on Silver Nanoparticles Loaded Gum Arabic Nanofibers. *Int J Biol Macromol* **2020**, *155*, 119–130. https://doi.org/10.1016/J.IJBIOMAC.2020.03.194.

22

(39) Blangiardo, A.; Lagomarsino, G.; Basso, A.; Canepa, P.; Cavalleri, O.; Rossi, S.; Monticelli, O. Preparation, Application and Recycling of a Catalytic Microflow Reactor Based on Polylactic Acid. *Appl Surf Sci* **2021**, *569*, 151019. https://doi.org/10.1016/J.APSUSC.2021.151019.

(40) Ferrari, P. F.; Pettinato, M.; Casazza, A. A.; De Negri Atanasio, G.; Palombo, D.; Perego, P. Polyphenols from Nerone Gold 26/6, a New Pigmented Rice, via Non-Conventional Extractions: Antioxidant Properties and Biological Validation. *Journal of Chemical Technology & Biotechnology* **2021**, *96* (6), 1691–1699. https://doi.org/10.1002/JCTB.6694.

(41) Meng, W.; Dong, Y.; Li, J.; Cheng, L.; Zhang, H.; Wang, C.; Jiao, Y.; Xu, J.; Hao, J.; Qu, H. Bio-Based Phytic Acid and Tannic Acid Chelate-Mediated Interfacial Assembly of Mg(OH)2 for Simultaneously Improved Flame Retardancy, Smoke Suppression and Mechanical Properties of PVC. *Compos B Eng* **2020**, *188*, 107854. https://doi.org/10.1016/J.COMPOSITESB.2020.107854.

(42) Wei, Z.; Peng, G.; Zhao, Y.; Chen, S.; Wang, R.; Mao, H.; Xie, Y.; Zhao, C. Engineering Antioxidative Cascade Metal-Phenolic Nanozymes for Alleviating Oxidative Stress during Extracorporeal Blood Purification. *ACS Nano* **2022**, *16* (11), 18329–18343. https://doi.org/10.1021/ACSNANO.2C06186/SUPPL_FILE/NN2C06186_SI_001.PDF.

(43) Liu, T.; Ma, M.; Ali, A.; Liu, Q.; Bai, R.; Zhang, K.; Guan, Y.; Wang, Y.; Liu, J.; Zhou, H. Self-Assembled Copper Tannic Acid Nanoparticles: A Powerful Nano-Bactericide by Valence Shift of Copper. *Nano Today* **2024**, *54*, 102071. https://doi.org/10.1016/J.NANTOD.2023.102071.

(44) Biesinger, M. C. Advanced Analysis of Copper X-Ray Photoelectron Spectra. *Surface and Interface Analysis* **2017**, *49* (13), 1325–1334. https://doi.org/10.1002/SIA.6239.

(45) Xi, J.; Wei, G.; An, L.; Xu, Z.; Xu, Z.; Fan, L.; Gao, L. Copper/Carbon Hybrid Nanozyme: Tuning Catalytic Activity by the Copper State for Antibacterial Therapy. *Nano Lett* **2019**, *19* (11), 7645–7654. https://doi.org/10.1021/ACS.NANOLETT.9B02242/SUPPL_FILE/NL9B02242_SI_001.PDF.

(46) Huang, Y.; Zhong, H.; Jiang, C.; Yang, J.; Zhang, J.; Zhao, F.; Liu, C. Copper-Based Nanomaterials as Peroxidase Candidates for Intelligent Colorimetric Detection and Antibacterial Applications. *Particuology* **2024**, *84*, 126–135. https://doi.org/10.1016/J.PARTIC.2023.03.009.

(47) Xia, Z.; Singh, A.; Kiratitanavit, W.; Mosurkal, R.; Kumar, J.; Nagarajan, R. Unraveling the Mechanism of Thermal and Thermo-Oxidative Degradation of Tannic Acid. *Thermochim Acta* **2015**, *605*, 77–85. https://doi.org/10.1016/J.TCA.2015.02.016.

(48) Deniz, A.; Zaytoun, N.; Hetjens, L.; Pich, A. Polyphosphazene-Tannic Acid Colloids as Building Blocks for Bio-Based Flame-Retardant Coatings. *ACS Appl Polym Mater* **2020**, *2* (12), 5345–5351. https://doi.org/10.1021/ACSAPM.0C00574/SUPPL_FILE/AP0C00574_SI_004.MP4.

(49) Zhao, Y.; Wang, J.; Chen, S.; Wei, Z.; Xie, Y.; Zhao, C. Polyphenol-Assisted Albumin-Based Biomineralization Nanocarriers with NIR-II-Targeted Photothermal Performance towards Broad-Spectrum Radical Scavenging. *J Mater Chem B* **2023**, *11* (23), 5108–5116. https://doi.org/10.1039/D3TB00541K.

(50) Li, Y.; Fu, R.; Zhu, C.; Fan, D. An Antibacterial Bilayer Hydrogel Modified by Tannic Acid with Oxidation Resistance and Adhesiveness to Accelerate Wound Repair. *Colloids Surf B Biointerfaces* **2021**, *205*, 111869. https://doi.org/10.1016/J.COLSURFB.2021.111869.

(51) Ninan, N.; Forget, A.; Shastri, V. P.; Voelcker, N. H.; Blencowe, A. Antibacterial and Anti-Inflammatory PH-Responsive Tannic Acid-Carboxylated Agarose Composite Hydrogels for Wound Healing. *ACS Appl Mater Interfaces* **2016**, *8* (42), 28511–28521. https://doi.org/10.1021/ACSAMI.6B10491/SUPPL_FILE/AM6B10491_SI_001.PDF.

(52) Farha, A. K.; Yang, Q. Q.; Kim, G.; Li, H. Bin; Zhu, F.; Liu, H. Y.; Gan, R. Y.; Corke, H. Tannins as an Alternative to Antibiotics. *Food Biosci* **2020**, *38*, 100751. https://doi.org/10.1016/J.FBIO.2020.100751.

(53) Ji, X.; Li, R.; Jia, W.; Liu, G.; Luo, Y.; Cheng, Z. Co-Axial Fibers with Janus-Structured Sheaths by Electrospinning Release Corn Peptides for Wound Healing. *ACS Appl Bio Mater* **2020**, *3* (9), 6430–6438. https://doi.org/10.1021/ACSABM.0C00860/ASSET/IMAGES/LARGE/MT0C00860_0010.JPEG.

(54) Das, P.; Ganguly, S.; Margel, S.; Gedanken, A. Immobilization of Heteroatom-Doped Carbon Dots onto Nonpolar Plastics for Antifogging, Antioxidant, and Food Monitoring Applications. *Langmuir* **2021**, *37* (11), 3508–3520. https://doi.org/10.1021/ACS.LANGMUIR.1C00471/ASSET/IMAGES/LARGE/LA1C00471_0009.JPEG.

(55) Du, X.; Hou, Y.; Wu, L.; Li, S.; Yu, A.; Kong, D.; Wang, L.; Niu, G. An Anti-Infective Hydrogel Adhesive with Non-Swelling and Robust Mechanical Properties for Sutureless Wound Closure. *J Mater Chem B* **2020**, *8* (26), 5682–5693. https://doi.org/10.1039/D0TB00640H.

(56) Vestby, L. K.; Grønseth, T.; Simm, R.; Nesse, L. L. Bacterial Biofilm and Its Role in the Pathogenesis of Disease. *Antibiotics 2020, Vol. 9, Page 59* **2020**, *9* (2), 59. https://doi.org/10.3390/ANTIBIOTICS9020059.

(57) Du, J.; Zhang, X.; Li, W.; Wang, M.; Zhou, X.; Ren, L. Generalized Multifunctional Coating Strategies Based on Polyphenol-Amine-Inspired Chemistry and Layer-by-Layer Deposition for Blood Contact Catheters. *ACS Biomater Sci Eng* **2024**, *10*, 3068. https://doi.org/10.1021/ACSBIOMATERIALS.4C00578/ASSET/IMAGES/LARGE/AB4C00578_0007.JPEG.

(58) Fan, G.; Cottet, J.; Rodriguez-Otero, M. R.; Wasuwanich, P.; Furst, A. L. Metal-Phenolic Networks as Versatile Coating Materials for Biomedical Applications. *ACS Appl Bio Mater* **2022**, *5* (10), 4687–4695. https://doi.org/10.1021/ACSABM.2C00136/ASSET/IMAGES/LARGE/MT2C00136_0004.JPEG.

(59) Dong, Z.; Zhao, J.; Xu, J.; Deng, W.; Sun, P. Strongly Adhesive, Self-Healing, Hemostatic Hydrogel for the Repair of Traumatic Brain Injury. *Biomacromolecules* **2023**. https://doi.org/10.1021/ACS.BIOMAC.3C01406/ASSET/IMAGES/LARGE/BM3C01406_0009.JPEG.

(60) Shokri, M.; Kharaziha, M.; Tafti, H. A.; Dalili, F.; Aghdam, R. M.; Eslaminejad, M. B. Engineering Wet-Resistant and Osteogenic Nanocomposite Adhesive to Control Bleeding and Infection after Median Sternotomy. *Adv Healthc Mater* **2024**, 2304349. https://doi.org/10.1002/ADHM.202304349.

(61) Ghuglot, R.; Titus, W.; Agnihotri, A. S.; Krishnakumar, V.; Krishnamoorthy, G.; Marimuthu, N. Stable Copper Nanoparticles as Potential Antibacterial Agent against Aquaculture Pathogens and Human Fibroblast Cell Viability. *Biocatal Agric Biotechnol* **2021**, *32*, 101932. https://doi.org/10.1016/J.BCAB.2021.101932.